

FPGA-based disturbance-observer servo for broadband noise suppression in laser frequency stabilization

Meung Ho Seo,¹ Jae Hoon Lee,² Young-Ho Park,¹ Hyun-Gue Hong,¹ Seji Kang,¹ Myoung-Sun Heo,¹ Sang-Bum Lee,² Taeg Yong Kwon,² Sangwon Seo,² and Sang Eon Park^{1,*}

¹*Time and Frequency Group, Korea Research Institute of Standards and Science, Daejeon 34113, Republic of Korea*

²*Atomic Quantum Sensing Group, Korea Research Institute of Standards and Science, Daejeon 34113, Republic of Korea*

(Dated: May 26, 2026)

We have demonstrated broadband frequency-noise suppression in a laser stabilization system by augmenting a conventional proportional-integral-derivative (PID) controller with a digital disturbance observer (DOB) implemented on a field-programmable gate array (FPGA). The DOB employs a first-order exponential moving average filter as its Q-filter, replacing multi-parameter frequency-domain plant identification with a single one-dimensional gain sweep. Using modulation transfer spectroscopy on the ⁸⁷Rb D₂ line at 780.24 nm, we have measured the frequency-noise power spectral density and the Allan deviation of the beat note between two independently stabilized lasers. The integrated rms frequency noise below 40 kHz decreased by 16.9 dB compared with PID alone, corresponding to a reduction from approximately 140 kHz to 20 kHz. The short-term fractional frequency instability improved from $\sigma_y(1\text{ ms}) = 7.9 \times 10^{-12}$ to 4.6×10^{-12} , while the long-term stability at $\tau > 1\text{ s}$ remained within statistical uncertainty. This DOB-augmented architecture offers a simple and effective route to enhanced noise rejection in FPGA-based servo systems for atomic physics experiments.

INTRODUCTION

Precise and reliable laser frequency stabilization is an essential prerequisite for a wide range of experiments in atomic, molecular, and optical (AMO) physics. Optical atomic clocks [1], atomic fountain clocks [2, 3], atom interferometers [4], quantum sensors [5], and trapped-ion quantum processors [6] all rely on laser sources whose frequency noise must be suppressed to levels dictated by the specific application requirements. As these technologies mature toward field-deployable instruments—including transportable optical clocks [7], quantum gravimeters [8], space-borne atom interferometers [9], compact satellite references [10], and portable atom-interferometry laser systems [11]—the demand for compact, robust, and high-performance laser stabilization systems has grown significantly.

The standard approach to laser frequency stabilization is the proportional-integral-derivative (PID) controller [12], typically implemented either in analog electronics or, more recently, on field-programmable gate arrays (FPGAs) [13–18]. While PID controllers are well understood and straightforward to tune, it is difficult to achieve sufficient loop gain at intermediate frequencies—above the unity-gain bandwidth of the integrator but below the closed-loop servo bandwidth—without compromising phase margin. External disturbances in this frequency range, arising from acoustic vibrations, mechanical resonances, or electronic pickup, can degrade the frequency noise power spectral density (PSD) [19, 20] and consequently the short-term frequency instability.

The disturbance observer (DOB) is a robust control technique introduced by Ohnishi and colleagues for motion control of mechatronic systems [21]. Subsequently

formalized within a two-degree-of-freedom control framework by Umeno and Hori [22], the DOB has become a standard tool in motion control [23, 24], robotics, and precision positioning [25], as reviewed comprehensively by Chen *et al.* [26] and Sariyildiz *et al.* [27]. The essential idea is to estimate the lumped disturbance acting on a plant by comparing the measured output with the output predicted from a nominal plant model, filtering the difference through a low-pass Q-filter, and feeding back the filtered estimate to cancel the disturbance. Crucially, Shim and Jo [28] have shown that robust stability can be guaranteed even when the nominal plant model is only approximate, provided that the Q-filter bandwidth is chosen conservatively. This property makes DOB particularly attractive for laser frequency stabilization, where the plant transfer function (from control voltage to optical frequency) is difficult to identify precisely due to the interplay of current modulation, thermal effects, and mechanical compliance of the laser cavity.

Although related model-based and feed-forward approaches have been applied to adjacent precision-control problems [29, 30], an explicit Q-filter DOB has not been widely deployed in optical frequency stabilization. The present work introduces such a DOB with the inverse plant model reduced to a single scalar gain K_n and an FPGA bit-shift implementation that uses no DSP slices. In this work, we have implemented a digital DOB alongside a PID controller on a Red Pitaya STEMLab 125-14 LN FPGA platform, operating at a clock frequency of 125 MHz. The Q-filter is realized as a simple first-order exponential moving average (EMA) filter, requiring only a single tunable parameter (the cutoff frequency) and no prior identification of the plant transfer function. Using modulation transfer spectroscopy (MTS) on the ⁸⁷Rb D₂

transition at 780.24 nm [31–33], we have characterized the frequency-noise power spectral density (PSD) and the overlapping Allan deviation [34, 35] of the beat note between two independently stabilized laser systems. We have found that the DOB reduces the integrated rms frequency noise below 40 kHz by approximately 17 dB compared with PID alone, confirming the low-pass nature of the disturbance rejection.

THEORY

The feedback system considered here consists of two controllers acting on the error signal $e(t)$: a conventional PID controller and a DOB. We first describe the operating principle of each in continuous-time, then discuss the frequency-domain properties of the combined system.

A PID controller produces a control signal u_{PID} from the error signal $e(t) = r(t) - y(t)$, where $r(t)$ is the set-point and $y(t)$ is the measured output. In the Laplace domain, the controller transfer function is

$$C(s) = K_p + \frac{K_i}{s} + K_d s, \quad (1)$$

where K_p , K_i , and K_d are the proportional, integral, and derivative gains, respectively. The proportional term responds instantaneously to the current error, the integral term accumulates past errors to eliminate steady-state offset, and the derivative term acts on the rate of change to provide phase lead. At low frequencies the integrator dominates the loop gain and is primarily responsible for eliminating steady-state offset, while the proportional and derivative terms extend the servo bandwidth to higher frequencies. However, the achievable PID loop gain at intermediate frequencies is limited by the requirement to maintain adequate phase margin, so external disturbances at these frequencies are only partially suppressed.

The disturbance observer addresses this limitation by adding a parallel inner loop that estimates and compensates for the lumped disturbance $d(t)$ acting on the plant. Consider the control system shown in Fig. 1: the PID controller $C(s)$ produces the nominal control signal u_{PID} , which is combined with the DOB correction to form the plant input u_{out} . The plant $P(s)$ converts u_{out} into the output $y(t)$, which is corrupted by the lumped disturbance $d(t)$:

$$Y(s) = P(s)U_{\text{out}}(s) + D(s), \quad (2)$$

where $Y(s)$, $U_{\text{out}}(s)$, and $D(s)$ are the Laplace transforms of the output, control input, and disturbance, respectively.

The DOB estimates $d(t)$ using a nominal model $P_n(s)$ of the plant. If $P_n(s)$ were an exact replica of $P(s)$, one could recover the disturbance simply as $\hat{D} = P_n^{-1}Y -$

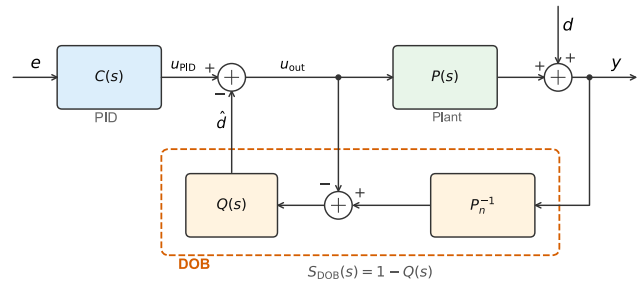


FIG. 1. Block diagram of the PID+DOB control architecture. The PID controller $C(s)$ generates the control signal u_{PID} from the error e . The plant $P(s)$ converts the input u_{out} to the output y , which is corrupted by the disturbance d . The DOB inner loop (dashed box) estimates d by passing $P_n^{-1}y - u_{\text{out}}$ through the Q-filter $Q(s)$, and subtracts the estimate \hat{d} from the control signal. The DOB sensitivity function $S_{\text{DOB}}(s) = 1 - Q(s)$ determines the low-pass disturbance rejection.

U_{out} . In practice, however, $P_n^{-1}(s)$ may be improper (more zeros than poles), and high-frequency noise would be amplified. The Q-filter $Q(s)$ resolves this by low-pass filtering the disturbance estimate:

$$\hat{D}(s) = Q(s) [P_n^{-1}(s)Y(s) - U_{\text{out}}(s)]. \quad (3)$$

The compensated control signal is then

$$U_{\text{out}}(s) = U_{\text{PID}}(s) - \hat{D}(s), \quad (4)$$

which closes the inner disturbance-rejection loop around the PID controller.

The key design parameter is the Q-filter, which determines the frequency range over which disturbances are rejected. A first-order low-pass filter with cutoff frequency ω_c is a convenient choice—unity gain at DC, monotonic roll-off, and a single tunable parameter:

$$Q(s) = \frac{\omega_c}{s + \omega_c}, \quad (5)$$

with $|Q(j\omega)| = 1$ at DC and rolling off to zero above ω_c . Assuming a perfect nominal model ($P_n = P$), the closed-loop transfer function from disturbance d to output y in the presence of the DOB can be expressed via the sensitivity function

$$S_{\text{DOB}}(s) = 1 - Q(s). \quad (6)$$

This function fully characterizes the DOB's disturbance rejection. Defining the cutoff frequency as $f_c = \omega_c/2\pi$, at frequencies $f \ll f_c$, $|Q| \approx 1$ and $|S_{\text{DOB}}| \ll 1$, so disturbances are strongly suppressed. At $f \gg f_c$, $|Q| \approx 0$ and $|S_{\text{DOB}}| \approx 1$, so the DOB becomes transparent and does not interfere with the PID controller. This frequency-selective behavior is the central advantage of the DOB—it adds noise rejection at frequencies below the Q-filter cutoff f_c , where PID gain alone is limited, while leaving

the high-frequency response unchanged. The DOB thus functions as a low-pass augmentation of the existing PID loop.

A further important property concerns the choice of the nominal plant model $P_n(s)$. In many practical situations the exact plant transfer function is difficult to identify. However, the Q-filter inherently limits the DOB's action to low frequencies, so the model P_n need only be accurate where $Q(s)$ is significant. If the plant can be approximated as a simple gain at frequencies below f_c , the inverse model reduces to a scalar multiplication $P_n^{-1}(s) \approx K_n$, and Eq. (3) simplifies to

$$\hat{D}(s) = Q(s)[K_n Y(s) - U_{\text{out}}(s)]. \quad (7)$$

The essential DOB structure—Q-filtered estimation of the lumped disturbance—and the sensitivity function $S_{\text{DOB}}(s) = 1 - Q(s)$ remain approximately valid under this simplification, at frequencies where $P(s) \approx P_0$.

The PID+DOB architecture maps efficiently onto digital hardware. In a sampled-data system with clock frequency f_{clk} , the PID controller is implemented as a parallel sum of proportional, integral (accumulator), and derivative (first difference) paths—a standard digital realization requiring only multiplications and additions per clock cycle.

The DOB has an even simpler digital form. The Q-filter of Eq. (5) is realized as a first-order exponential moving average (EMA) filter:

$$q[n] = (1 - \alpha)q[n-1] + \alpha x[n], \quad (8)$$

where $x[n] = K_n y[n] - u_{\text{out}}[n]$ is the raw disturbance estimate and α is the smoothing parameter. Choosing α as a power of two, $\alpha = 2^{-n}$, eliminates the need for a hardware multiplier: the product $\alpha \cdot x$ becomes a right bit-shift by n positions. The Q-filter cutoff frequency, in the small- α limit, is then

$$f_c = \frac{2^{-n} f_{\text{clk}}}{2\pi}, \quad (9)$$

controlled by the single integer parameter n . The entire DOB computation per clock cycle—gain, subtraction, and EMA filtering—reduces to additions and bit-shifts with no floating-point arithmetic, making field-programmable gate array (FPGA) implementation straightforward. The PID and DOB paths execute in parallel at the full sampling rate, with a fixed pipeline latency that we quantify in Sec. .

EXPERIMENTAL SETUP

The experimental apparatus consists of three subsystems: the spectroscopy optics for generating the MTS error signal, the FPGA-based digital servo for PID and

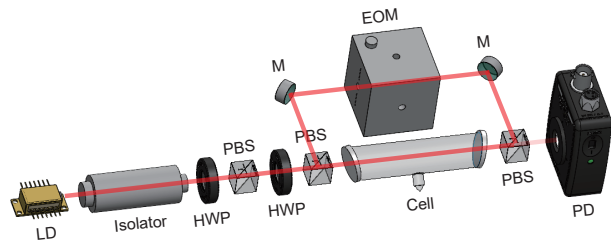


FIG. 2. Optical layout of the modulation transfer spectroscopy system. The pump beam is phase-modulated at 5 MHz and counter-propagates through the ^{87}Rb vapor cell with the unmodulated probe beam. LD: laser diode, HWP: half-wave plate, PBS: polarizing beam splitter, M: mirror, EOM: electro-optic modulator, PD: photodetector.

DOB feedback, and the measurement instruments for characterizing frequency noise and stability.

The spectroscopy system employs modulation transfer spectroscopy [31, 32, 36] on the ^{87}Rb D₂ transition ($F = 2 \rightarrow F' = 3$, $\lambda = 780.24$ nm) in a vapor cell (Thorlabs GC19075-RB87). The laser source is an external-cavity diode laser (Eagleyard miniECL) driven by a compact low-noise laser controller (Koheron CTL200-1). A 5 MHz phase modulation is applied to the pump beam via an electro-optic modulator (Qubig PM7-NIR), while the unmodulated probe beam counter-propagates through the cell. The probe beam power is 150 μW with a $1/e^2$ intensity radius of 3 mm, and the pump beam power is 4.5 mW with a $1/e^2$ intensity radius of 6 mm. The probe beam is detected by an amplified photodetector (Thorlabs PDA10A2). The optical layout of the MTS spectroscopy is shown in Fig. 2.

The digital servo system is built on two Red Pitaya STEMLab 125-14 LN platforms, each featuring a Xilinx Zynq-7010 system-on-chip with dual 14-bit 125 MHz analog-to-digital and digital-to-analog converters. The detector output is routed through a bias tee (Mini-Circuits ZFBT-6GW+) and a low-noise amplifier (Mini-Circuits ZFL-500LN+) to the first unit (RP#1), which performs modulation and demodulation: a direct-digital-synthesis module generates the 5 MHz carrier that drives the EOM, and a digital lock-in demodulator extracts the dispersive MTS error signal from the detector output. The demodulated error signal is transmitted from RP#1 RF OUT2 to the second unit (RP#2) via a coaxial cable.

Both RP#1 and RP#2 implement their respective digital signal-processing functions in custom Verilog RTL. The block diagrams of Fig. 3(b) are one-to-one graphical representations of these RTLs, with each block corresponding to a Verilog module and the signal arrows corresponding to the synthesized data path. RP#2 in particular realizes the PID+DOB architecture described in Sec. II.

The DOB Q-filter is implemented as the EMA of

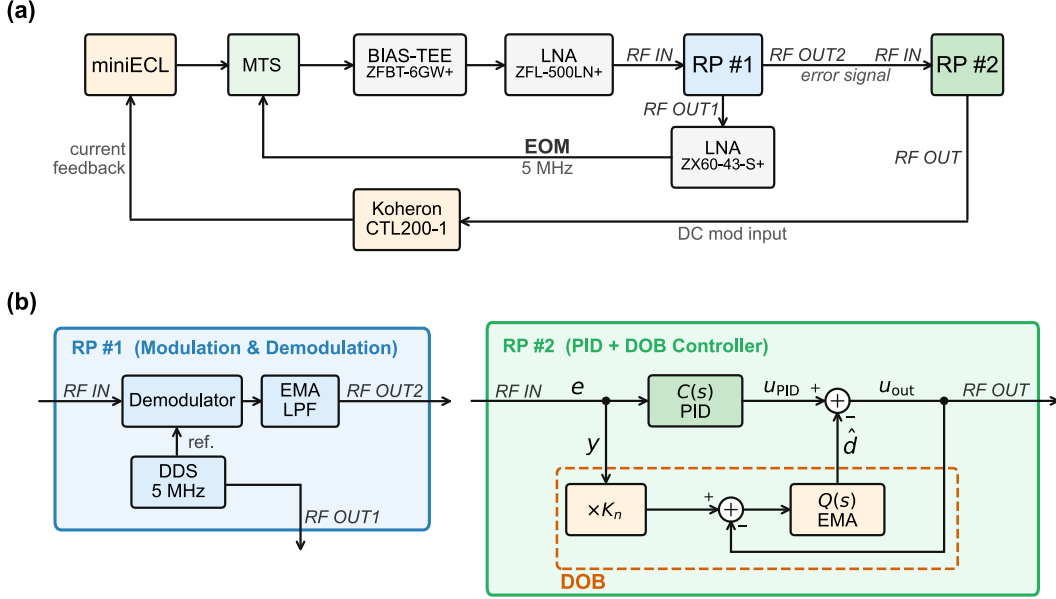


FIG. 3. Electronic signal flow diagram of the FPGA-based PID+DOB servo system. (a) External signal path connecting the optical and electronic subsystems. (b) Internal block diagrams of RP#1 and RP#2. The DOB inner loop in RP#2 implements the simplified form of Eq. (7), where the inverse plant model P_n^{-1} of the general DOB architecture (Fig. 1) is replaced by the scalar gain K_n .

Eq. (8) with default cutoff $n = 9$, giving $f_c \approx 39$ kHz. The DOB pipeline (five clock cycles, 40 ns) contributes only 0.56° of phase lag at f_c , well within the robust-stability margin of Shim and Jo [28]. The combined output $u_{\text{out}} = u_{\text{PID}} - \hat{d}$ drives the DC current modulation input of the Koheron CTL200-1 laser controller. The electronic signal flow is illustrated in Fig. 3. Comparing the DOB inner loop in Fig. 3(b) with the general architecture of Fig. 1, the inverse plant model $P_n^{-1}(s)$ is replaced by a single gain element K_n . At low frequencies, all analog components (specified above) have cutoffs far exceeding f_c and contribute essentially flat response. The cascaded plant $P(s)$ is therefore dominated by the digital low-pass filters of the lock-in demodulator (≈ 1.24 MHz) and the PID EMA pre-filters (≈ 310 kHz), whose cutoffs both lie well above f_c . Hence $P(s) \approx P_0$ and $P_n^{-1}(s) \approx K_n$. The disturbance estimate is then computed as Eq. (7), and the DOB sensitivity function $S_{\text{DOB}}(s) = 1 - Q(s)$ remains approximately valid in this regime. This design-driven constant-gain approximation, together with the conservative Q-filter bandwidth, replaces the multi-parameter frequency-domain plant identification of conventional DOB designs with a single one-dimensional gain sweep on K_n (demonstrated experimentally in Sec.).

To characterize the frequency noise PSD, we have recorded the MTS error signal with an FFT signal analyzer (Thorlabs PNA-1). The analyzer employs 18-bit analog-to-digital conversion across a measurement band-

width of DC to 3 MHz, with a noise floor below 60 nV/ $\sqrt{\text{Hz}}$. The error signal voltage is converted to frequency units using the discriminator slope, obtained from the linear region of MTS waveforms recorded at different laser currents and calibrated against the manufacturer’s specified wavelength tuning coefficient for the Eagleyard miniECL ($d\lambda/dI \approx 0.001$ nm/mA). For Allan deviation measurements, we have constructed a beat-note setup using two independent, nominally identical MTS-stabilized laser systems. One beam is frequency-shifted by 100 MHz using a fiber-coupled acousto-optic modulator (Aerodiode 780AOM.1), and the two beams are combined in a 50:50 fiber coupler (Thorlabs PN780R5A2), with each laser contributing approximately 200 μW of optical power at the coupler input. The frequency of the beat note is detected by a photodetector (Thorlabs PDA10A2) and measured by a frequency counter (Keysight 53230A) operated in continuous gap-free frequency measurement mode, enabling proper Allan deviation computation with no dead time between gate intervals. In this mode the gate time is adjustable from 10 μs to 1000 s in 10 μs steps, with up to 10^6 samples per acquisition stored in the instrument’s internal memory. We have used two complementary configurations: a short-term measurement with a 1 ms gate time and 10^6 gap-free samples (total duration 1000 s), and a long-term measurement with a 1 s gate time and 2.3×10^4 gap-free samples (total duration ~ 6.4 h).

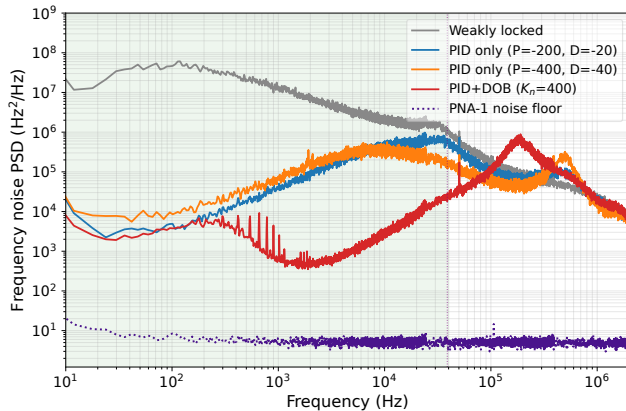


FIG. 4. Frequency-noise PSD of the MTS error signal for four operating conditions: weakly locked baseline (gray), PID only (blue), high-gain PID only (orange), and PID+DOB (red). See text for the gain settings. The PNA-1 noise floor (purple dotted) shows the signal analyzer’s intrinsic limit. The green shaded region marks the integration window (up to 40 kHz). The dotted vertical line marks the Q-filter cutoff at 39 kHz. Discrete peaks visible across all traces are residual power-line harmonics.

RESULTS

Figure 4 compares the frequency-noise PSD under four operating conditions: a weakly locked baseline (integrator only at minimum gain), approximating the free-running laser; PID only ($K_p = -200$, $K_i = -200$, $K_d = -20$); high-gain PID only ($K_p = -400$, $K_d = -40$); and PID+DOB ($K_p = -200$, $K_i = -200$, $K_d = -20$, $K_n = 400$). The PID gains were tuned to just below the onset of sustained closed-loop (servo) oscillation. The high-gain trace shows the loop being pushed past this limit into a developed servo bump.

The weakly locked baseline shows a broad frequency-noise pedestal of order 10^6 Hz²/Hz across DC–100 kHz. With PID alone (blue/orange traces), the integrator strongly suppresses noise below 100 Hz, leaving a residual broadband frequency noise that extends up to ~ 40 kHz, peaking near 24 kHz at the closed-loop servo bump set by the joint action of all PID terms. Higher PID gains (orange trace) only reshape this residual noise (integrated rms drops only ~ 3 dB) before exciting a developed servo bump that drives the loop into oscillation, so PID alone cannot remove this residual noise without instability. A more elaborate digital-filter design might mitigate this, but at the cost of multi-parameter tuning.

Engaging the DOB—added in parallel without re-tuning the PID—reduces the PSD across this region by nearly two orders of magnitude: the integrated rms frequency noise below 40 kHz drops by 16.9 dB, from approximately 140 kHz (PID only) to approximately 20 kHz (PID+DOB). Below $f_c \approx 39$ kHz the suppression is max-

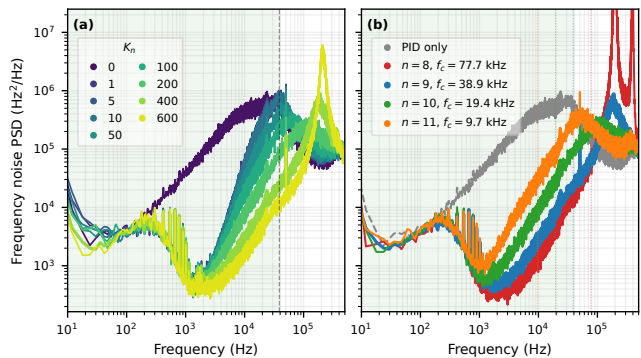


FIG. 5. Dependence of the frequency-noise PSD on DOB parameters. (a) DOB gain sweep ($K_n = 0$ –600, dark to light, viridis colormap) at fixed Q-filter cutoff $n = 9$. The dashed line marks $f_c = 39$ kHz. (b) Q-filter cutoff sweep ($n = 8$ –11) at fixed gain $K_n = 400$. PID only (gray) is shown for reference. Dotted lines mark f_c for each n . The green shaded regions indicate the integration window (up to 40 kHz).

imal. Above f_c , traces with and without DOB converge, confirming the low-pass rejection predicted by Eq. (6). A relocated servo bump appears near 200 kHz, above the 40 kHz integration upper bound. The DOB raises the loop gain below f_c , and the combined system’s high-frequency response—shaped by the Q-filter rolloff (above f_c) and the PID pre-filter cutoff at ~ 310 kHz—develops a new closed-loop resonance between these two scales, observed at ~ 200 kHz. The signal-analyzer noise floor (PNA-1) is shown for reference.

The two DOB parameters are characterized by orthogonal sweeps (Fig. 5). At fixed $n = 9$ (Fig. 5a), every K_n trace exhibits the characteristic $|S_{\text{DOB}}| = |1 - Q|$ shape predicted by Eq. (6)—maximal suppression below f_c , transparent above—with the suppression depth growing monotonically with K_n , from 1.8 dB ($K_n = 1$) to 19.8 dB ($K_n = 600$). At higher K_n the excess above f_c also grows as the strengthened inner-loop response extends toward the PID pre-filter cutoff, signalling the eventual onset of instability. At fixed $K_n = 400$ (Fig. 5b), varying $n = 8$ –11 shifts the suppression bandwidth from $f_c = 9.7$ kHz to 77.7 kHz, in agreement with Eq. (9). At the smallest n tested ($n = 8$) the relocated servo bump enters the 50 kHz to 500 kHz region, reaching the PID pre-filter cutoff (~ 310 kHz, Sec.), and the loop oscillates.

Figure 6 shows the time-domain stability via the Allan deviation [34] $\sigma_y(\tau)$ of the beat note between two independently stabilized laser systems. With PID only, $\sigma_y(1 \text{ ms}) = 7.9 \times 10^{-12}$. Engaging the DOB improves this to 4.6×10^{-12} (factor of 1.7). At $\tau = 1 \text{ s}$ the Allan deviations are 1.05×10^{-12} (PID only) and 1.09×10^{-12} (PID+DOB). The DOB’s short-term improvement corresponds to the low-frequency PSD reduction shown in Fig. 4 (quantitatively cross-validated below), while

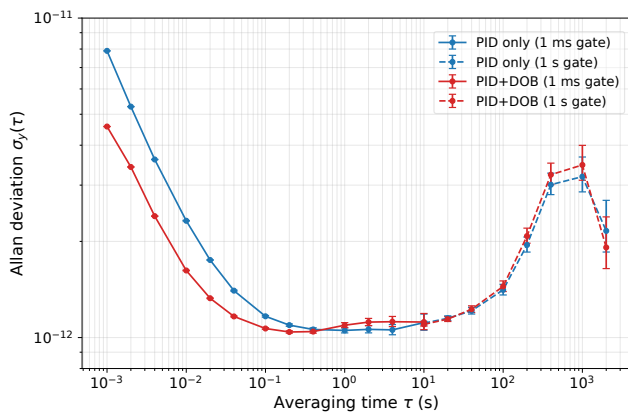


FIG. 6. Allan deviation of the beat-note frequency. Short-term data (solid lines, 1 ms gate) and long-term data (dashed lines, 1 s gate) are shown for PID only (blue) and PID+DOB (red).

at long τ the integrator alone already suppresses low-frequency noise to the asymptotic floor, leaving no residual disturbance for the DOB to address. Both traces share a bump near $\tau \sim 1000$ s from periodic laboratory temperature fluctuations, common to both configurations.

Finally, we cross-validate by integrating the measured PSD with the standard transfer function [35]:

$$\sigma_y^2(\tau) = \frac{2}{\nu_{\text{opt}}^2} \int_0^\infty S_\nu(f) \frac{\sin^4(\pi f \tau)}{(\pi f \tau)^2} df. \quad (10)$$

Single-laser predictions are $\sigma_y(1 \text{ ms}) \approx 1.1 \times 10^{-11}$ (PID only) and 3.7×10^{-12} (PID+DOB). For two independent lasers the expected beat-note values are $\sqrt{2}$ times these, i.e., 1.6×10^{-11} and 5.2×10^{-12} . The measured $\sigma_y(1 \text{ ms}) = 7.9 \times 10^{-12}$ and 4.6×10^{-12} agree with the predictions to within a factor of two, providing internal cross-validation of the DOB-induced reduction.

CONCLUSION

We have demonstrated a digital DOB applied to laser frequency stabilization. A digital DOB, implemented as a first-order EMA Q-filter on a Red Pitaya STEMLab 125-14 LN FPGA, was combined with a conventional PID controller to stabilize a 780.24 nm external-cavity diode laser to the ^{87}Rb D₂ transition via modulation transfer spectroscopy. The DOB reduced the integrated rms frequency noise below 40 kHz by 16.9 dB—from approximately 140 kHz to 20 kHz—and improved the short-term Allan deviation at $\tau = 1$ ms from 7.9×10^{-12} to 4.6×10^{-12} , a factor of 1.7. At $\tau = 1$ s the Allan deviations are 1.05×10^{-12} (PID only) and 1.09×10^{-12} (PID+DOB), unchanged by the DOB. At long τ the integrator alone already suppresses the low-frequency noise

to the asymptotic floor, leaving no residual disturbance for the DOB to address. Together with the factor-of-1.7 short-term improvement at $\tau = 1$ ms, this confirms the low-pass action of the DOB.

The principal advantage of this approach lies in its simplicity. Higher-order integral controllers can also achieve similar suppression in a comparable frequency range, but at the cost of multi-parameter tuning and additional pipeline latency. The DOB instead reduces tuning to a single K_n sweep, keeps $|1 - Q|$ bounded by unity (no inner-loop amplification), and adds only five clock cycles (40 ns, $\sim 0.6^\circ$ at f_c) of latency, occupying 1836 LUTs and 527 flip-flops with no additional block RAM or DSP slices. The constant-gain approximation $P_n^{-1} \approx K_n$, enabled by the deliberately flat analog chain, removes the need for explicit plant identification, while the entire DOB computation reduces to additions and bit-shifts with no floating-point arithmetic.

These characteristics are particularly relevant for field-deployable atomic sensors [7, 8], where compactness, robustness, and minimal hardware overhead are essential. Future work will explore higher-order Q-filters for steeper roll-off characteristics and extension to multi-input/multi-output configurations for simultaneous frequency and intensity stabilization.

This work was supported by funding from the Korea government (KASA, Korea Aerospace Administration; grant number RS-2022-00165802) and by the Measurement Technology for Grand National Strategic Industries program funded by the Korea Research Institute of Standards and Science (KRISS 2026-GP2026-0012). The authors declare no conflicts of interest. Data underlying the results presented in this paper are available from the corresponding author upon reasonable request.

* parkse@kriss.re.kr

- [1] A. D. Ludlow, M. M. Boyd, J. Ye, E. Peik, and P. O. Schmidt, Optical atomic clocks, *Rev. Mod. Phys.* **87**, 637 (2015).
- [2] R. Wynands and S. Weyers, Atomic fountain clocks, *Metrologia* **42**, S64 (2005).
- [3] S. Bize, P. Laurent, M. Abgrall, H. Marion, I. Maksimovic, L. Cacciapuoti, J. Grünert, C. Vian, F. Pereira dos Santos, P. Rosenbusch, P. Lemonde, G. Santarelli, P. Wolf, A. Clairon, A. Luiten, M. Tobar, and C. Salomon, Cold atom clocks and applications, *J. Phys. B* **38**, S449 (2005).
- [4] M. Kasevich and S. Chu, Atomic interferometry using stimulated Raman transitions, *Phys. Rev. Lett.* **67**, 181 (1991).
- [5] K. Bongs, M. Holynski, J. Vovrosh, P. Bouyer, G. Condon, E. Rasel, C. Schubert, W. P. Schleich, and A. Roura, Taking atom interferometric quantum sensors from the laboratory to real-world applications, *Nat. Rev. Phys.* **1**, 731 (2019).
- [6] C. D. Bruzewicz, J. Chiaverini, R. McConnell, and J. M.

- Sage, Trapped-ion quantum computing: Progress and challenges, *Appl. Phys. Rev.* **6**, 021314 (2019).
- [7] J. Grotti, S. Koller, S. Vogt, S. Hafner, U. Sterr, C. Lisdat, H. Denker, C. Voigt, L. Timmen, A. Rolland, F. N. Baynes, H. S. Margolis, M. Zampaolo, P. Thoumany, M. Pizzocaro, B. Rauf, F. Bregolin, A. Tampellini, P. Barbieri, M. Zucco, G. A. Costanzo, C. Clivati, F. Levi, and D. Calonico, Geodesy and metrology with a transportable optical clock, *Nat. Phys.* **14**, 437 (2018).
- [8] V. Ménoret, P. Vermeulen, N. Le Moigne, S. Bonvalot, P. Bouyer, A. Landragin, and B. Desruelle, Gravity measurements below $10^{-9}g$ with a transportable absolute quantum gravimeter, *Sci. Rep.* **8**, 12300 (2018).
- [9] D. Becker, M. D. Lachmann, S. T. Seidel, H. Ahlers, A. N. Dinkelaker, J. Grosse, O. Hellmig, H. Müntinga, V. Schkolnik, T. Wendrich, A. Wenzlawski, B. Weps, R. Corgier, T. Franz, N. Gaaloul, W. Herr, D. Lüdtke, M. Popp, S. Amri, H. Duncker, M. Erbe, A. Kohfeldt, A. Kubelka-Lange, C. Braxmaier, E. Charron, W. Ertmer, M. Krutzik, C. Lämmerzahl, A. Peters, W. P. Schleich, K. Sengstock, R. Walser, A. Wicht, P. Windpassinger, and E. M. Rasel, Space-borne Bose–Einstein condensation for precision interferometry, *Nature* **562**, 391 (2018).
- [10] A. Strangfeld, S. Kanthak, M. Schiemangk, B. Wiegand, A. Wicht, A. Ling, and M. Krutzik, A prototype of a compact rubidium-based optical frequency reference for operation on nanosatellites, *J. Opt. Soc. Am. B* **38**, 1885 (2021).
- [11] M. Schmidt, M. Prevedelli, A. Giorgini, G. M. Tino, and A. Peters, A portable laser system for high-precision atom interferometry experiments, *Appl. Phys. B* **102**, 11 (2011).
- [12] J. Bechhoefer, Feedback for physicists: A tutorial essay on control, *Rev. Mod. Phys.* **77**, 783 (2005).
- [13] T. Preuschoff, M. Schlosser, and G. Birkel, Digital laser frequency and intensity stabilization based on the STEM-lab platform (originally Red Pitaya), *Rev. Sci. Instrum.* **91**, 083001 (2020).
- [14] B. Wiegand, B. Leykauf, R. Jördens, and M. Krutzik, Linien: A versatile, user-friendly, open-source FPGA-based tool for frequency stabilization and spectroscopy parameter optimization, *Rev. Sci. Instrum.* **93**, 063001 (2022).
- [15] L. Neuhaus, M. Croquette, R. Metzdrorf, S. Chua, P.-E. Jacquet, A. Journeaux, A. Heidmann, T. Briant, T. Jacquemin, P.-F. Cohadon, and S. Deléglise, Python Red Pitaya Lockbox (PyRPL): An open source software package for digital feedback control in quantum optics experiments, *Rev. Sci. Instrum.* **95**, 033003 (2024).
- [16] V. Avalos, X. Nie, A. Yang, C. He, S. Kumar, and K. Dieckmann, Field-programmable-gate-array-based digital frequency stabilization of low-phase-noise diode lasers, *Rev. Sci. Instrum.* **94**, 063001 (2023).
- [17] D. R. Leibbrandt and J. Heidecker, An open source digital servo for atomic, molecular, and optical physics experiments, *Rev. Sci. Instrum.* **86**, 123115 (2015).
- [18] J. Appel, A. MacRae, and A. I. Lvovsky, A versatile digital GHz phase lock for external cavity diode lasers, *Meas. Sci. Technol.* **20**, 055302 (2009).
- [19] G. Di Domenico, S. Schilt, and P. Thomann, Simple approach to the relation between laser frequency noise and laser line shape, *Appl. Opt.* **49**, 4801 (2010).
- [20] K. Numata, A. Kemery, and J. Camp, Thermal-noise limit in the frequency stabilization of lasers with rigid cavities, *Phys. Rev. Lett.* **93**, 250602 (2004).
- [21] K. Ohnishi, M. Shibata, and T. Murakami, Motion control for advanced mechatronics, *IEEE/ASME Trans. Mechatron.* **1**, 56 (1996).
- [22] T. Umeno and Y. Hori, Robust speed control of DC servomotors using modern two degrees-of-freedom controller design, *IEEE Trans. Ind. Electron.* **38**, 363 (1991).
- [23] C. J. Kempf and S. Kobayashi, Disturbance observer and feedforward design for a high-speed direct-drive positioning table, *IEEE Trans. Control Syst. Technol.* **7**, 513 (1999).
- [24] E. Schrijver and J. van Dijk, Disturbance observers for rigid mechanical systems: equivalence, stability, and design, *ASME J. Dyn. Syst. Meas. Control* **124**, 539 (2002).
- [25] E. Sariyildiz and K. Ohnishi, A guide to design disturbance observer, *ASME J. Dyn. Syst. Meas. Control* **136**, 021011 (2014).
- [26] W.-H. Chen, J. Yang, L. Guo, and S. Li, Disturbance-observer-based control and related methods—an overview, *IEEE Trans. Ind. Electron.* **63**, 1083 (2016).
- [27] E. Sariyildiz, R. Oboe, and K. Ohnishi, Disturbance observer-based robust control and its applications: 35th anniversary overview, *IEEE Trans. Ind. Electron.* **67**, 2042 (2020).
- [28] H. Shim and N. H. Jo, An almost necessary and sufficient condition for robust stability of closed-loop systems with disturbance observer, *Automatica* **45**, 296 (2009).
- [29] Y.-X. Chao, Z.-X. Hua, X.-H. Liang, Z.-P. Yue, L. You, and M. K. Tey, Pound–drever–hall feedforward: laser phase noise suppression beyond feedback, *Optica* **11**, 945 (2024).
- [30] L. Li, W.-W. Huang, X. Wang, Y.-L. Chen, and L. Zhu, Periodic-disturbance observer using spectrum-selection filtering scheme for cross-coupling suppression in atomic force microscopy, *IEEE Trans. Autom. Sci. Eng.* **20**, 2037 (2023).
- [31] J. H. Shirley, Modulation transfer processes in optical heterodyne saturation spectroscopy, *Opt. Lett.* **7**, 537 (1982).
- [32] D. J. McCarron, S. A. King, and S. L. Cornish, Modulation transfer spectroscopy in atomic rubidium, *Meas. Sci. Technol.* **19**, 105601 (2008).
- [33] H.-R. Noh, S. E. Park, L. Z. Li, J.-D. Park, and C.-H. Cho, Modulation transfer spectroscopy for ^{87}Rb atoms: theory and experiment, *Opt. Express* **19**, 23444 (2011).
- [34] D. W. Allan, Statistics of atomic frequency standards, *Proc. IEEE* **54**, 221 (1966).
- [35] D. W. Allan, Time and frequency (time-domain) characterization, estimation, and prediction of precision clocks and oscillators, *IEEE Trans. Ultrason. Ferroelectr. Freq. Control* **34**, 647 (1987).
- [36] S. Lee, G. Moon, S. E. Park, H.-G. Hong, J. H. Lee, S. Seo, T. Y. Kwon, and S.-B. Lee, Laser frequency stabilization in the 10^{-14} range via optimized modulation transfer spectroscopy on the ^{87}Rb D₂ line, *Opt. Lett.* **48**, 1020 (2023).